Nano Energy 77 (2020) 105189

Contents lists available at ScienceDirect

Nano Energy

journal homepage: http://www.elsevier.com/locate/nanoen

# Elucidating dual-defect mechanism in rhenium disulfide nanosheets with multi-dimensional ion transport channels for ultrafast sodium storage

Wei Zong [a], Chao Yang [d], Lulu Mo [a], Yue Ouyang [a], Hele Guo [a], Lingfeng Ge [f], Yue-E. Miao [a], Dewei Rao [e], Jiangwei Zhang [c,**], Feili Lai [b,*], Tianxi Liu [a,***]

[a] State Key Laboratory for Modification of Chemical Fibers and Polymer Materials, College of Materials Science and Engineering, Innovation Center for Textile Science and Technology, Donghua University, Shanghai, 201620, PR China
[b] Department of Chemistry, KU Leuven, Celestijnenlaan 200F, Leuven, 3001, Belgium
[c] Dalian National Laboratory for Clean Energy & State Key Laboratory of Catalysis, Dalian Institute of Chemical Physics, Chinese Academy of Sciences (CAS), Dalian, 116023, PR China
[d] Institute of Materials Science and Technology, Technische Universität Berlin, Straße des 17. Juni, Berlin, 10623, Germany
[e] School of Materials Science and Engineering, Jiangsu University, Zhenjiang, 212013, PR China
[f] School of Chemistry, University of Bristol, Cantock's Close, Bristol, BS8 1TS, UK

ARTICLE INFO

*Keywords:*
Sodium storage
Sulfur vacancy
Interlayer defect
Carbonized bacterial cellulose
$ReS_2$

ABSTRACT

The sodium-ion storage property in two-dimensional transition metal dichalcogenides (TMDs) is still seriously confined due to the lacking of efficient pathways for $Na^+$ insertion, which enlightens the construction of multi-dimensional ion channels a necessary. Herein, we prepared interlayer defect, sulfur vacancy-contained $ReS_2$ nanosheets on porous nitrogen-doped carbonized bacterial cellulose (dr-$ReS_{2-x}$/NCBC). In such dual-defect configuration, the interlayer defects provide interconnected in-plane/interlamination channels for offering extra pathways of $Na^+$ insertion/extraction and shortening ionic diffusion distance, while the sulfur vacancy could further enhance the electronic conductivity and induce more active sites for $Na^+$ storage. Therefore, the dr-$ReS_{2-x}$/NCBC anode displays an enhanced rate capacity (231.2 mAh $g^{-1}$ at 5 A $g^{-1}$) and a good cycling stability (187.3 mAh $g^{-1}$ at 5 A $g^{-1}$ after 500 cycles). Furtherly revealed by density functional theory calculations, the sodium-ion storage property is attributed to its negatively shifted binding energy for sodium ions (from −0.771 to −1.791/-1.244 eV), and alleviated structural change (from 5.8% to 3.4%/-1.6%) during sodiation/desodiation processes. The dr-$ReS_{2-x}$/NCBC anode was also assembled coupling with $Na_3V_2(PO_4)_3$ cathode as a sodium-ion full cell for practical applications. This work is expected to offer an in-depth understanding between dual-defect engineering in TMDs-based anodes and as-enhanced sodium-storage performance.

## 1. Introduction

Rechargeable batteries are considered as one of the most promising renewable energy storage systems to relieve the environmental pollution and satisfy the increasing demand of sustainable energy resources owing to high energy density and effective energy conversion [1–5]. As compared with the widely used lithium-ion batteries (LIBs), sodium-ion batteries (SIBs) have obtained increasing attention for large-scale applications based on abundant natural resources. However, a critical problem before the commercialization and practical deployment of SIBs is the lack of suitable and stable electrodes. Among various two-dimensional (2D) materials, transition metal dichalcogenides (TMDs) are regarded as one of the most promising frameworks for efficient sodium-ion storage owing to their high theoretical capacity, appropriate interlayer space and good mechanical properties [6–9]. In spite of these advantages in TMDs, there are still three bottlenecks impeding their wide applications as electrodes for sodium-ion storage: 1) The larger ionic radius of $Na^+$ ($r = 1.02$ Å) would cause severe volume expansion in the stacked direction of TMDs layers during $Na^+$ insertion, resulting in poor cycling stability without long-time usage [10,11]; 2) A perfect crystal structure in 2D TMDs would dramatically decrease the number of active edges with restricted channels for both $Na^+$

* Corresponding author.
** Corresponding author.
*** Corresponding author.
*E-mail addresses:* jwzhang@dicp.ac.cn (J. Zhang), feili.lai@kuleuven.be (F. Lai), txliu@dhu.edu.cn (T. Liu).

https://doi.org/10.1016/j.nanoen.2020.105189
Received 4 June 2020; Received in revised form 29 June 2020; Accepted 8 July 2020
Available online 25 July 2020

insertion/extraction and diffusion; 3) The poor intrinsic conductivity of TMDs bulk brings out inferior electron transfer. These remaining challenges in TMDs result in their sluggish kinetics, low capacity, and poor rate stability as electrodes for sodium-ion storage, particularly under high current rates [12,13].

According to previous researches, one of the feasible solutions is to construct efficient ion channels in active materials for fast transport of alkali metal ions, such as regulation of interlayer spacing [14–16], construction of nanofluidic structures [17–19], and introduction of multi-phase heterostructures [20,21]. For example, Yu et al. created 2D nanofluidic channels by stacking ultrathin $Co_3O_4$ nanosheets for lithium-ion battery, featuring selective and fast Li-ion transport [18]. Liang et al. synthesized bimetallic selenide heterostructure ($CoSe_2$/ZnSe) with abundant phase boundaries, which shows fast diffusion kinetics and relieves the stress of $Na^+$ insertion for sodium-ion storage [20]. These studies enlighten us to fully exploit the advantages of layered structure in terms of TMDs and improve their storage performance by preferentially introducing defect structures. Among various defect structures, one-dimensional (1D) interlayer defect (also denoted as "line defect") could dig out additional channels as new pathways for ion insertion/extraction, and thus shorten the diffusion distance. Moreover, it is also highly desired to enhance the electron transport within each individual TMDs layers for high-rate capability, to circumvent which another defect structure of vacancy (also denoted as "point defect") is taken into consideration [22–28]. In detail, the as-introduced vacancy can not only manipulate the electronic structure, but also produce new active sites for efficient binding of alkali ions. For example, Ma et al. prepared $MoS_2$ with sulfur vacancies towards sodium-ion storage, from both experimental and theoretical analyses of which proved that the sulfur vacancies simultaneously improved the electronic conductivity of $MoS_2$ and endowed more active sites for $Na^+$ adsorption [29]. However, the controllable dual-defect modulation and understanding the mechanism between dual-defect engineering in TMDs-based anodes and their storage performance still remain challenging with lacked models for detailed investigation.

As a rising star toward sodium-ion storage among TMDs family, rhenium disulfide ($ReS_2$) possesses disordered stacking layers that formed by covalent Re–S bonds and extremely weak interlamellar forces from van der Waals interactions. This weak interlayer coupling makes the deformation and interlayer sliding of atomic layers not only possible but also easy, which is beneficial to facilitating the mobility of sodium ions, and alleviating the irreversible expansion of $ReS_2$ structure [30,31]. Thus, $ReS_2$ could be regarded as an ideal model to investigate the relationship between dual-defect engineering (between interlayer defect and sulfur vacancy) and sodium-ion storage performance. It stands to reason that a synergic strategy combining controlled interlayer defect and vacancy engineering may work towards $ReS_2$-based electrodes for sodium battery, whereas, the controllable dual-defect modulation and understanding the mechanism between dual-defect engineering in TMDs-based anodes and storage performance remain challenging without too much previous researches.

Herein, we prepared interlayer defect, sulfur vacancy-contained $ReS_2$ nanosheets on porous nitrogen-doped carbonized bacterial cellulose (dr-$ReS_{2-x}$/NCBC) by regulating the ratio between ammonium perrhenate and thiourea precursors during the hydrothermal reaction, and annealing treatment in Ar/$H_2$ atmosphere. From the individual aspects of dual-defects in dr-$ReS_{2-x}$/NCBC, the interlayer defect could provide interconnected ion transport channels for $Na^+$ insertion/extraction and shorten ionic diffusion distance, while the sulfur vacancy could not only enhance the electronic conductivity and ion binding ability, but also alleviate the volume change during sodiation/desodiation processes. As a result, the dr-$ReS_{2-x}$/NCBC delivers optimized pseudocapacitive effect and ion diffusion coefficient, leading to its high sodium storage capacity (421.2 mAh $g^{-1}$ at 0.2 A $g^{-1}$), good rate performance (231.2 mAh $g^{-1}$ at 5 A $g^{-1}$), and long-term cycling stability (187.3 mAh $g^{-1}$ at 5 A $g^{-1}$ after 500 cycles). As followed by density functional theory calculations, this enhanced electrochemical performance is attributed to its abrupt change of band structure from a semiconductor to conductors, negatively shifted binding energy for sodium ions (from −0.771 to −1.791/-1.244 eV), and alleviated structural change (from 5.8% to 3.4%/-1.6%). Meanwhile, the assembled sodium-ion full cells also display extraordinary performance with stable cycle life (capacity retention of 96.3% after 100 cycles) and rate capability (186.4 mAh $g^{-1}$ at 5 A $g^{-1}$).

## 2. Experimental section

**Synthesis of dr-$ReS_{2-x}$/NCBC.** Firstly, porous nitrogen-doped carbonized bacterial cellulose nanofibers (NCBC) were prepared according to the previous method [32–34]. Briefly, bacterial cellulose was soaked in 0.1 M NaOH solution for 6 h, and then washed with deionized water for several times to pH ≈ 7. Subsequently, the hydrous bacterial cellulose was frozen by liquid nitrogen and freeze-dried to obtain dried bacterial cellulose. Then, the dried bacterial cellulose is heated up to 800 °C with the assistance of urea ($CH_4N_2O$) in a nitrogen atmosphere with a heating rate of 5 °C $min^{-1}$, and maintained for 2 h to obtain NCBC nanofibers. Then, 1 mmol ammonium perrhenate ($NH_4ReO_4$) and 2.2 mmol thiourea ($C_2H_5NS$) (Re: S molar ratio = 1:2.2) were dissolved in 40 mL $H_2O$. After stirring for 30 min, 3 mmol hydroxylamine hydrochloride ($NH_2OH{\cdot}HCl$) was added to form a homogeneous solution. Furthermore, 10 mg NCBC nanofibers was immersed in the above solution, which was transferred into 80 mL Teflon-lined autoclave and maintained at 200 °C for 24 h. After cooling to room temperature, the defect-rich $ReS_2$ nanosheets with one-dimensional (1D) interlayer defects on NCBC (dr-$ReS_2$/NCBC) was rinsed with distilled water and ethanol for several time, and dried in a vacuum oven overnight. To obtain interlayer defect, sulfur vacancy-contained $ReS_2$ nanosheets on porous nitrogen-doped carbonized bacterial cellulose (dr-$ReS_{2-x}$/NCBC), the dr-$ReS_2$/NCBC was annealed at 450 °C for 2 h under Ar/$H_2$ (95%/5%) atmosphere. $ReS_2$/NCBC was obtained *via* same process of dr-$ReS_2$/NCBC, which the molar ratio of $NH_4ReO_4$ and $C_2H_5NS$ = 1:2. $ReS_2$ bulk was prepared *via* the same steps as $ReS_2$/NCBC without adding NCBC nanofibers.

**Electrochemical Measurements.** The as-prepared active materials, carbon black and polyvinylidene fluoride (PVDF) were dispersed in N-Methyl pyrrolidone solvent (NMP) with a mass ratio of 7:2:1. Then, the slurry was pasted on the current collector of copper foil, which was dried in a vacuum oven at 80 °C for 12 h. The mass loading in a tablet (ϕ = 12 mm) of the working electrode is 0.5–1 mg $cm^{-2}$. The coin cell (CR2025) was assembled in Ar-filled glovebox. Li or Na foil was served as the counter electrode, and Celgard 2400 membrane and glass fiber were used as separators for lithium-ion batteries (LIBs) and sodium-ion batteries (SIBs), respectively. The electrolytes for sodium-ion and lithium-ion storages are 1 mL $NaClO_4$ in EC/DEC (1:1 vol%) with FEC (5 vol %) and 1 mL $LiPF_6$ in EC/DMC/EMC (1:1:1 vol%), respectively. The galvanostatic charge/discharge were performed on a Land CT-2001A (Wuhan, China) Instruments testing system at room temperature, while the mass specific capacity was calculated based on the mass of the anode materials. The cyclic voltammetry (CV) was conducted using an Arbin Instruments testing system (Arbin-SCTS). The Electrochemical impedance spectroscop (EIS) were recorded on an electrochemical workstation (CHI 760D) in the frequency range of 0.01 Hz–100 kHz with an AC amplitude of 5 mV. In addition, all the cells were held at open circuits and room temperature for 12 h before electrochemical tests. For the Li/Na full cell, the cathode was fabricated by casting a slurry of $LiCo_2O_4$ and $Na_3V_2(PO_4)_3$, carbon black, and PVDF with a mass ratio of 7:2:1 in NMP solvent onto aluminum current collectors, which was dried in a vacuum oven at 80 °C overnight. The electrolyte and the separator performed in full cells were all the same as in half cells.

**Characterization.** The morphology of the samples was observed by field-emission scanning electron microscopy (FESEM, Ultra 55) and high-resolution transmission electron microscopy (HRTEM, Talos

F200S). X-ray diffraction (XRD) patterns were measured using an X'Pert Pro X-ray diffractometer equipped with Cu Kα radiation (λ = 0.1542 nm) at a current of 40 mA and voltage of 40 kV. X-ray photoelectron spectroscopy (XPS) analyses were made with a VG ESCALAB 220I-XL device. The curve fitting of all XPS spectra was accomplished using XPS Peak 4.1 software. All XPS spectra were calibrated according to the C 1s line at 284.8 eV, while curve fitting and background subtraction were accomplished using the RBD AugerScan 3.21 software provided by RBD Enterprises. Electron paramagnetic resonance (EPR) spectra were measured on an EPR spectrometer (JEOL JES-FA200) at 298 K. The X-ray absorption find structure spectra (Re $L_3$-edge) were collected at BL14W1 beamline of Shanghai Synchrotron Radiation Facility (SSRF). The data were collected in fluorescence mode while the corresponding reference sample were collected in transmission mode using a Lytle detector. The sample were grinded and uniformly daubed on the special adhesive tape. The acquired EXAFS data were processed according to the standard procedures using the ATHENA module of Demeter software packages. The EXAFS spectra were obtained by subtracting the post-edge background from the overall absorption and then normalizing with respect to the edge-jump step. Subsequently, the χ(k) data of were Fourier transformed to real (R) space using a hanning windows (dk = 1.0 $Å^{-1}$) to separate the EXAFS contributions from different coordination shells. To obtain the quantitative structural parameters around central atoms, least-squares curve parameter fitting was performed using the ARTEMIS module of Demeter software packages.

The following EXAFS equation was used:

$$\chi(k) = \sum_j \frac{N_j S_0^2 F_j(k)}{kR_i^2} \cdot \exp\left[-2k^2\sigma_j^2\right] \cdot \exp\left[\frac{-2R_j}{\lambda(k)}\right] \cdot \sin\left[2kR_j + \varphi_j(k)\right] \quad (1)$$

The theoretical scattering amplitudes, phase shifts and the photoelectron mean free path for all paths calculated. $S_0^2$ is the amplitude reduction factor, $F_j(k)$ is the effective curved-wave backscattering amplitude, $N_j$ is the number of neighbors in the jth atomic shell, $R_j$ is the distance between the Xray absorbing central atom and the atoms in the jth atomic shell (backscatterer), λ is the mean free path in Å, $\varphi_j(k)$ is the phase shift (including the phase shift for each shell and the total central atom phase shift), $\sigma_j$ is the Debye-Waller parameter of the jth atomic shell (variation of distances around the average $R_j$). The functions $F_j(k)$, λ and $\varphi_j(k)$ were calculated with the ab initio code FEFF9. The additional details for EXAFS simulations are given below.

All fits were performed in the *R* space with *k*-weight of 2 while phase correction was also applied in the first coordination shell to make R value close to the physical interatomic distance between the absorber and shell scatterer. The coordination numbers of model samples were fixed as the nominal values. The obtained $S_0^2$ was fixed in the subsequent fitting. While the internal atomic distances R, Debye-Waller factor $\sigma^2$, and the edge-energy shift Δ were allowed to run freely.

**Computational Methods.** Vienna ab initio simulation package (VASP) [35,36] was applied to perform all the first-principle density functional theory calculations with the Perdew-Burke-Ernzerhof generalized gradient approximation (GGA-PBE) [37,38]. The interaction of ion-electron is described by projected augmented wave (PAW) potentials [39]. The cutoff energy for the plane-wave expansion of electron wave function is set to be 600 eV in all the calculations. A 5 × 5 × 1 k-point mesh is adopted for sample the surface, and the convergence threshold was set as $10^{-5}$ eV in energy and $10^{-2}$ eV/Å in force.

## 3. Results and discussion

**Synthesis and structural characterization of the products.** The synthetic process of interlayer defect, sulfur vacancy-contained $ReS_2$ nanosheets on porous nitrogen-doped carbonized bacterial cellulose (dr-$ReS_{2-x}$/NCBC) is illustrated in Fig. 1a. Firstly, the bacterial cellulose (BC) hydrogel was undergone freeze-dried process to obtain the BC aerogel [40], which was further carbonized under a urea atmosphere to produce porous NCBC (Fig. 1b, Fig. S1). The defect-rich $ReS_2$ nanosheets with one-dimensional (1D) interlayer defects on NCBC (dr-$ReS_2$/NCBC) were obtained by regulating the ratio between ammonium perrhenate and thiourea precursors during the hydrothermal reaction. Attributing to the incorporation of three-dimensional (3D) NCBC substrate, the dr-$ReS_2$ nanosheets could distribute on its surface uniformly (Fig. S2) without obvious aggregation of $ReS_2$ bulk (Fig. S3). Subsequently, the dr-$ReS_2$/NCBC was annealed at 450 °C under Ar/$H_2$ (95:5) atmosphere to incorporate sulfur vacancies, which is denoted as dr-$ReS_{2-x}$/NCBC. The well-maintained morphology of dr-$ReS_{2-x}$/NCBC (Fig. 1c) indicates the annealing process only occurs on an atomic level. Transmission electron microscopy (TEM) images of dr-$ReS_{2-x}$/NCBC (Fig. 1d and e) demonstrate the uniform distribution of ultrathin dr-$ReS_{2-x}$ nanosheets, resulting in an integrity with average diameter of 80–100 nm. The diffraction ring in its selected area electron diffraction (SAED) pattern (Inset in Fig. 1d) is indexed to (100) planes of $ReS_2$, indicating the polycrystalline characteristic of dr-$ReS_{2-x}$ nanosheets. Line-scan energy-dispersive X-ray spectroscopy (LSEDS) persuasively proves that dr-$ReS_{2-x}$ nanosheets are homogenously coated on the outer surface of each individual porous carbon nanofiber (Inset in Fig. 1e), which is also confirmed by its EDS elemental mappings (Fig. 1f) with homogeneous distribution of each individual element (C, N, Re, and S) throughout the entire dr-$ReS_{2-x}$/NCBC. As the high-resolution scanning transmission electron microscopy (HRTEM) image shown in Fig. 1g, the characteristic *d*-spacing in dr-$ReS_{2-x}$/NCBC (0.65 nm) corresponds to the (100) lattice fringe of $ReS_2$. The interlayer distance of dr-$ReS_{2-x}$ nanosheets in dr-$ReS_{2-x}$/NCBC expands slightly to 0.65 nm as compared with that 0.61 nm in pristine $ReS_2$ bulk, which is in line with the X-ray diffraction (XRD) result (Figs. S4 and S5). More importantly, the successful generation of 1D interlayer defect is confirmed by the discontinuous crystal fringes of dr-$ReS_{2-x}$ nanosheets along the lamellar dimension (Fig. 1h and i), while the possibly incorporated sulfur vacancies in dr-$ReS_{2-x}$ nanosheets (Fig. 1j) were further confirmed by the following measurements.

Therefore, X-ray photoelectron spectroscopy (XPS), electron paramagnetic resonance (EPR), and synchrotron radiation technology were conducted for both dr-$ReS_{2-x}$/NCBC and dr-$ReS_2$/NCBC to determine their difference in electronic structures. Firstly, the characteristic element peaks of Re, S, C and N are observed in the XPS survey spectra of dr-$ReS_{2-x}$/NCBC and dr-$ReS_2$/NCBC (Fig. 2a). Meanwhile, negative shifts of 0.1 eV are observed in both S $2p_{1/2}$ and S $2p_{3/2}$ peaks of dr-$ReS_{2-x}$/NCBC when compared to the dr-$ReS_2$/NCBC sample (Fig. 2b), which can be ascribed to the successful introduction of sulfur vacancy [41–43]. As the EPR spectra shown in Fig. 2c, the dr-$ReS_{2-x}$/NCBC shows a strong signal at $g = 2.002$, which is caused by the trapped electrons from the sulfur vacancy in dr-$ReS_{2-x}$ nanosheets [44–46]. Furthermore, X-ray absorption fine structure (XAFS) spectroscopy was used to investigate the difference of local coordination structures owing to sulfur vacancy. The Re $L_3$-edge X-ray absorption near edge structure (XANES) spectrum of the dr-$ReS_{2-x}$ nanosheets (Fig. 2d) shows slight difference as compared to that of the dr-$ReS_2$ nanosheets, which was further verified by corresponding Fourier transform extended X-ray absorption fine structure (FT-EXAFS) spectra (Fig. 2e). In detail, the peaks at 2.24 Å correspond to the Re–S bonds in both dr-$ReS_{2-x}$ and dr-$ReS_2$ nanosheets, where the peak intensity of dr-$ReS_{2-x}$ decreases significantly as compared to the dr-$ReS_2$, originating from the formation of sulfur vacancy for the Re partial rearrangement. From the corresponding oscillation functions $\kappa^2\chi(k)$ spectra (Fig. S8), the dr-$ReS_{2-x}$ presents slightly reduced oscillation amplitude, suggesting correlative structural differences in the local atomic environment. The aforementioned results prove the highly incorporated sulfur vacancy in dr-$ReS_{2-x}$ once more, with more detailed quantitative coordination configurations of Re in the Supplementary information (Fig. S&S10, Table S1). The EXAFS data fitting results show that the coordination number of Re–S bond in dr-$ReS_{2-x}$ (N = 1.55) is smaller than that in dr-$ReS_2$ (N = 3.57), which demonstrate that partial S atoms have been escaped successfully in the dr-$ReS_{2-x}$ crystal after

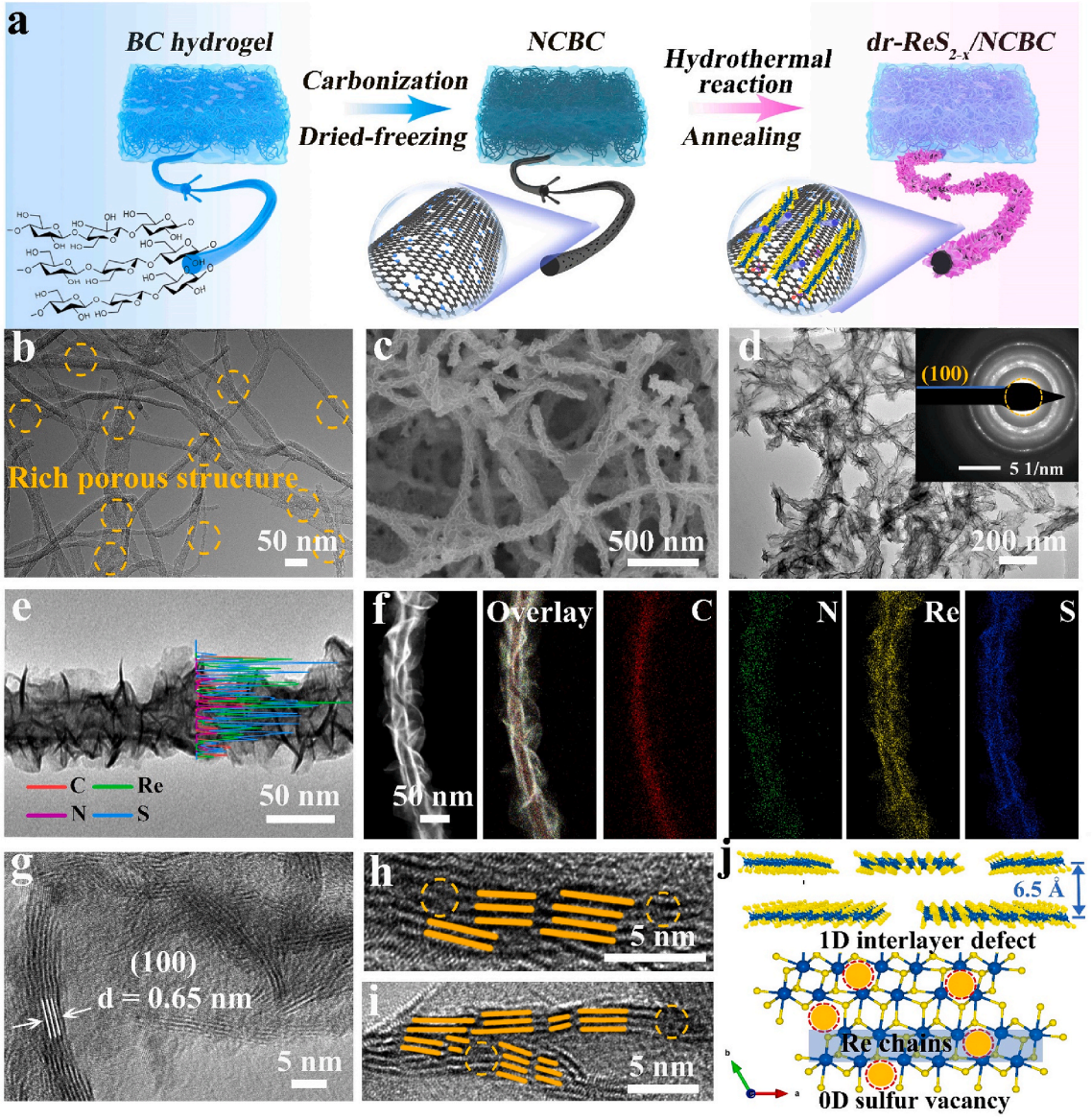


**Fig. 1.** a) Schematic illustration of the synthesis process for dr-$ReS_{2-x}$/NCBC. b) TEM image of NCBC. c) SEM image of dr-$ReS_{2-x}$/NCBC. d) TEM image of dr-$ReS_{2-x}$/NCBC (Inset: SAED pattern). e) The line-scan TEM-EDS analysis for dr-$ReS_{2-x}$/NCBC. f) HAADF-STEM image and corresponding element mappings for C, N, Re and S elements in dr-$ReS_{2-x}$/NCBC. g) HRTEM image of dr-$ReS_{2-x}$/NCBC. h, i) Cross-sectional HRTEM images of dr-$ReS_{2-x}$/NCBC. j) Schematic illustration for one-dimensional interlayer defect and zero-dimensional sulfur vacancy in dr-$ReS_{2-x}$.

annealing under Ar/$H_2$ atmosphere. Meanwhile, the sulfur vacancy in dr-$ReS_{2-x}$ can also be confirmed from its slightly reduced scattering intensity of Re–S bond, as shown in the wavelet transform (WT) of dr-$ReS_{2-x}$ and dr-$ReS_2$ (Fig. 2f) [45,47,48]. The exact experimental chemical compositions of dr-$ReS_{2-x}$/NCBC and dr-$ReS_2$/NCBC were characterized by EDS (Table S2), manifesting segmental sulfur atoms were removed during the thermal annealing process.

**Electrochemical performance.** In order to reveal the relationship between dual-defect structure (interlayer defect and sulfur vacancy) and sodium-ion storage performance, the dr-$ReS_{2-x}$/NCBC, dr-$ReS_2$/NCBC, $ReS_2$/NCBC, and $ReS_2$ bulk were prepared as anodes in Na-ion half devices. Fig. 3a shows the cyclic voltammetry (CV) profiles of dr-$ReS_{2-x}$/NCBC during its initial five cycles, where the potential window is between 0.01 and 3 V (*vs.* $Na^+$/Na) with a scan rate of 0.1 mV $s^{-1}$. Two pronounced reduction peaks are detected at 1.21 and 0.42 V in the first cycle, which are caused from the sodiation reaction of $ReS_2$ with the generation of Re and $Na_2S$ phases, as well as the formation of irreversible solid electrolyte interphase (SEI) layer. In the following cycles, two distinct oxidation peaks at 1.45/1.95 V can be assigned to the stepwise desodiation reaction of formed Re and $Na_2S$. Additionally, the reduction peaks observed at 1.91/0.87 V can be attributed to the conversion reaction from $ReS_2$ to metallic Re and $Na_2S$ [49,50]. To be noted, the CV profiles after the first cycle show excellent reversibility, indicating the electrochemical reactions in dr-$ReS_{2-x}$/NCBC are highly reversible. Fig. 3b shows the galvanostatic charge-discharge (GCD) profiles of various samples, where the dr-$ReS_{2-x}$/NCBC exhibits not only elongated voltage platform but also much smaller polarization, proving its highly improved reversibility during sodiation/desodiation processes. The dr-$ReS_{2-x}$/NCBC shows highest capacity among the four samples, which is calculated to be 421.2, 376.7, 323.1, and 276.4 mAh $g^{-1}$ as the current density increases from 0.2 to 2 A $g^{-1}$ (Fig. 3c), as well as a high capacity of 231.2 mAh $g^{-1}$ even at a high current density of 5 A $g^{-1}$. Markedly, the reversible capacity of dr-$ReS_{2-x}$/NCBC can be recovered to 386.5 mAh $g^{-1}$ when the current density returns to 0.2 A $g^{-1}$. The capacity at 5 A $g^{-1}$ for dr-$ReS_{2-x}$/NCBC is about 1.3, 1.8 and 7.6 times higher than those for dr-$ReS_2$/NCBC, $ReS_2$/NCBC and $ReS_2$ bulk, respectively.

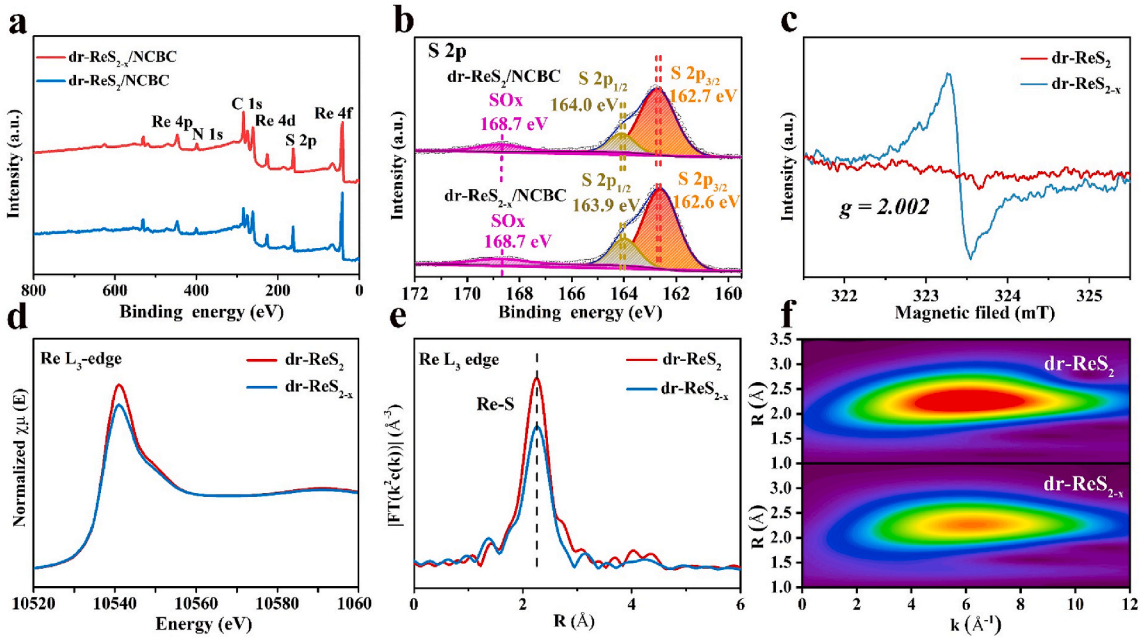


**Fig. 2.** a) XPS survey spectra of dr-$ReS_2$/NCBC and dr-$ReS_{2-x}$/NCBC. b) High-resolution S 2p XPS spectra of dr-$ReS_{2-x}$/NCBC and dr-$ReS_2$/NCBC. c) EPR spectra of dr-$ReS_2$ and dr-$ReS_{2-x}$. d) XANES spectra for Re $L_3$-edges, and e) its Fourier transformed (FT) spectra of dr-$ReS_2$ and dr-$ReS_{2-x}$. f) Wavelet transform (WT)-XAFS of dr-$ReS_2$ and dr-$ReS_{2-x}$.

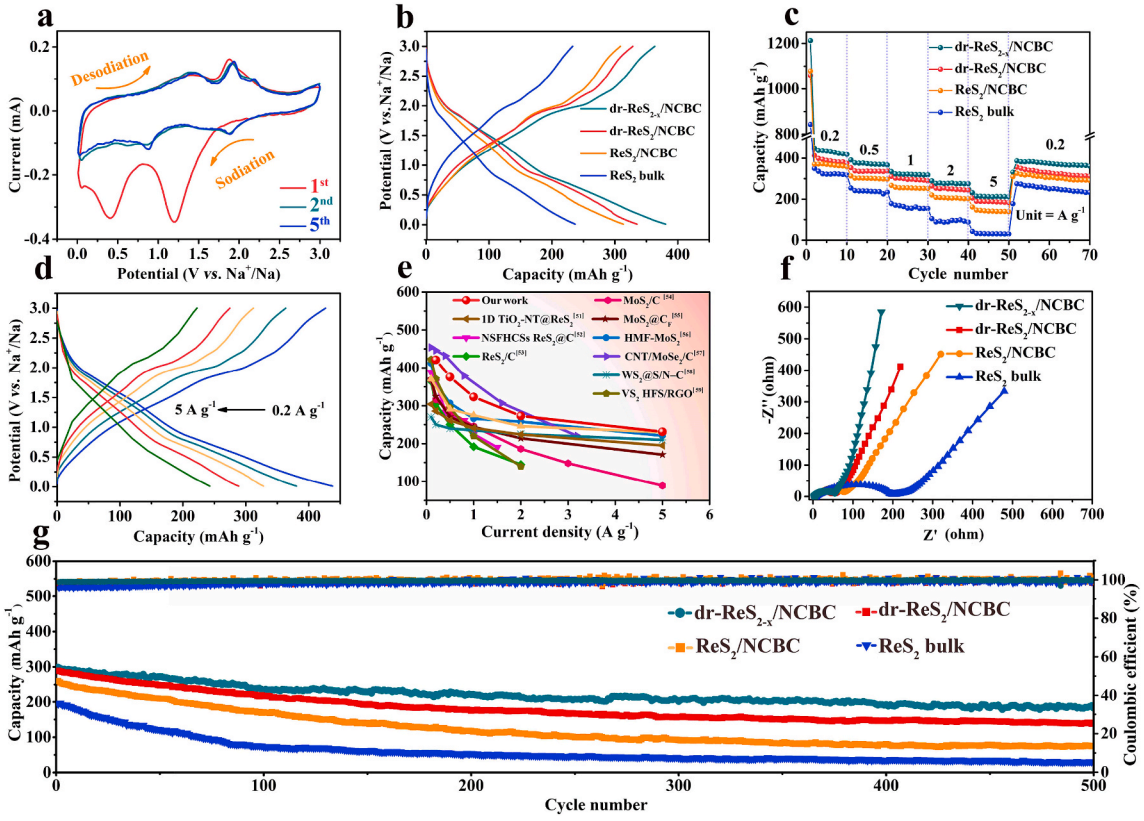


**Fig. 3.** Electrochemical performance of various anodes in sodium-ion half battery: a) CV curves for dr-$ReS_{2-x}$/NCBC in the first five cycles at 0.1 mV $s^{-1}$. b) GCD profiles, and c) rate capability of dr-$ReS_{2-x}$/NCBC, dr-$ReS_2$/NCBC, $ReS_2$/NCBC and $ReS_2$ bulk. d) GCD profiles of dr-$ReS_{2-x}$/NCBC at various current densities. e) Comparison of the sodium-ion storage performance of dr-$ReS_{2-x}$/NCBC, as well as previously reported TMD-based materials. f) EIS curves, and g) cycling performance of dr-$ReS_{2-x}$/NCBC, dr-$ReS_2$/NCBC, $ReS_2$/NCBC and $ReS_2$ bulk in 5 A $g^{-1}$.

Moreover, the dr-$ReS_{2-x}$/NCBC show better capacity retention (0.2–5 A $g^{-1}$) of 54.9% as compared to that of dr-$ReS_2$/NCBC (51.9%) and $ReS_2$/NCBC (44.2%), indicating its superior capability. The superior rate capability of dr-$ReS_{2-x}$/NCBC can be confirmed from its well-preserved GCD curves (Fig. 3d) with inconspicuous capacity loss as the current density increases, which implies its ultrafast reaction kinetics even upon high charge/discharge rates. Notably, the rate capability of dr-$ReS_{2-x}$/NCBC is better than those of previously reported TMDs-based materials for sodium storage (Fig. 3e, Table S3) [51–59]. Electrochemical impedance spectroscopy (EIS) analysis of various samples (Fig. 3f) manifests that dr-$ReS_{2-x}$/NCBC possesses much lower charge-transfer resistance ($R_{ct}$ = 51.2 Ω) as compared to those of dr-$ReS_2$/NCBC ($R_{ct}$ = 53.8 Ω), $ReS_2$/NCBC ($R_{ct}$ = 79.3 Ω), and $ReS_2$ bulk ($R_{ct}$ = 204.1 Ω). In the low-frequency region, the higher slope gradient of dr-$ReS_{2-x}$/NCBC implies its capacitive-like behavior and accelerated sodium ion diffusion, which are attributed to its enhanced electronic conductivity after the incorporation of the NCBC substrate and dual-defect structure engineering. For these same advantages, the dr-$ReS_{2-x}$/NCBC displays a remarkably enhanced long-term stability (187.3 mAh $g^{-1}$ after 500 cycles under 5 A $g^{-1}$) as shown in Fig. 3g. More importantly, the dual-defect engineering, including interlayer defect and sulfur vacancy, also works towards other alkali-ion batteries (lithium-ion storage) with detailed discussion (Fig. S11).

Up to now, the reaction kinetic behavior in a dual-defect contained TMDs-based anode still remains veiled, which is deeply investigated by using dr-$ReS_{2-x}$/NCBC as a platform. Fig. 4a shows the CV curves of dr-$ReS_{2-x}$/NCBC at different scan rates (0.1–0.5 mV $s^{-1}$). Notably, the redox peaks of the dr-$ReS_{2-x}$/NCBC show much larger area and smaller polarization than the other three electrodes (Fig. 4b, Fig. S12), indicating its faster reaction kinetics across the whole anode. When compared to the CV curve of dr-$ReS_2$/NCBC at 0.5 mV $s^{-1}$, the oxidation peak in the CV curve of dr-$ReS_{2-x}$/NCBC shifts from 1.61 to 1.56 V, while the reduction peak shifts from 0.72 to 0.76 V (Fig. 4c). This reduced potential difference in the CV curve of dr-$ReS_{2-x}$/NCBC indicates its enhanced redox reaction kinetics due to the incorporation of abundant sulfur vacancies. As the linear relation between $I_p$ and $v^{1/2}$ shown in Fig. 4d, the slopes for dr-$ReS_{2-x}$/NCBC are 1.14 (Peak 1) and −0.92 (Peak 3), respectively, which are much higher than those in dr-$ReS_2$/NCBC (Peak 1: 0.81, Peak 3: -0.58), $ReS_2$/NCBC (Peak 1: 0.72, Peak 3: -0.49), and $ReS_2$ bulk (Peak 1: 0.47, Peak 3: -0.39) (Fig. S13). According to the correlation between the peak current ($i$) and scan rate ($v$) obtained from the CV curves, the $b$ value could be calculated by the following equations:

$$i = ab^{v} \tag{2}$$

$$\log(i) = b\log(v) + \log(a) \tag{3}$$

where $a$ and $b$ are adjustable parameters that can be calculated by the linear relationship between the log($i$) versus log($v$) plots. Generally, if the $b$ value is close to 0.5, the electrochemical behavior is dominated by a diffusion-controlled process, while the $b$ value approaches to 1.0, the pseudocapacitive behavior is the main charge storage process. As shown

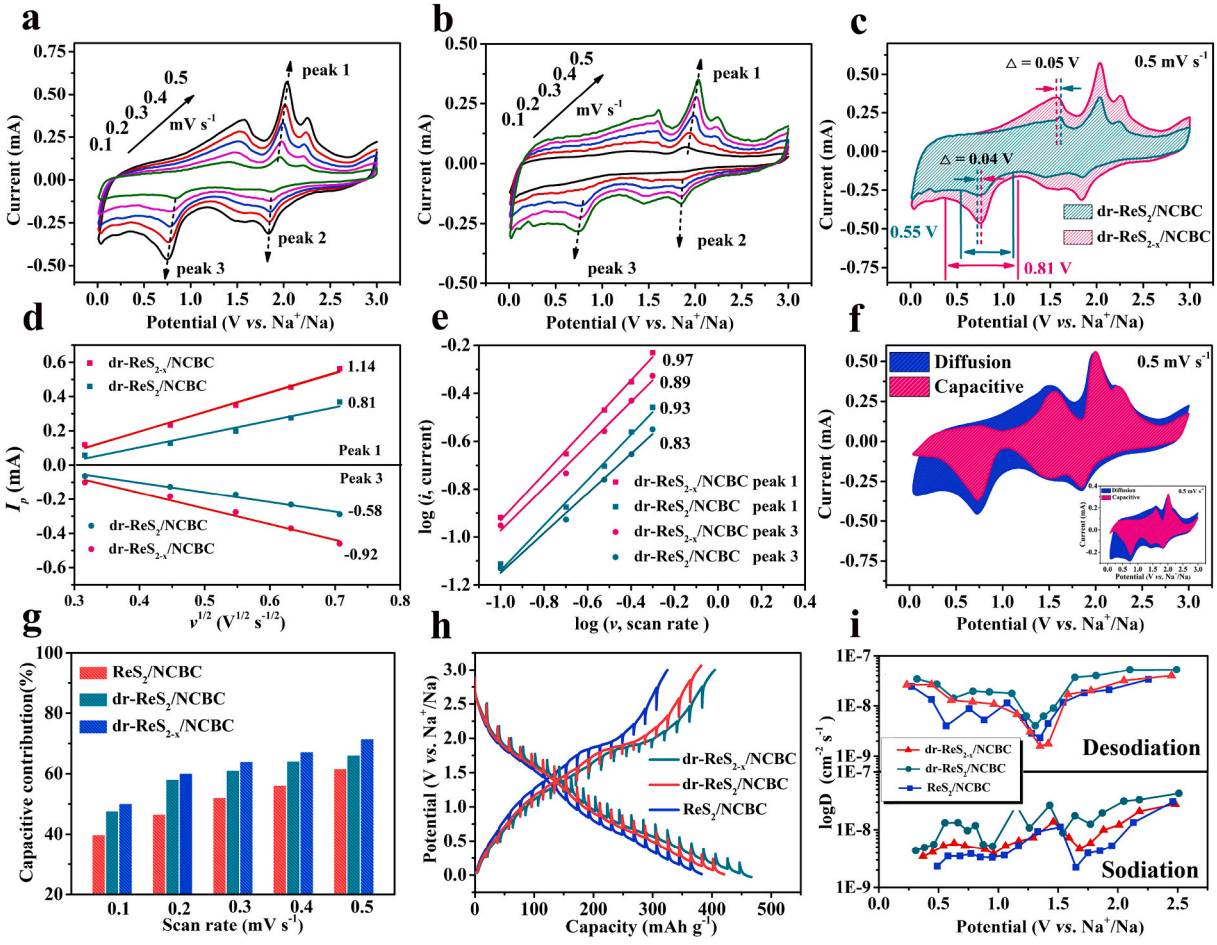


**Fig. 4.** The CV curves at stepwise scan rates (0.1, 0.2, 0.3, 0.4, and 0.5 mV $s^{-1}$) for a) dr-$ReS_{2-x}$/NCBC, and b) dr-$ReS_2$/NCBC. c) The CV curves of dr-$ReS_{2-x}$/NCBC and dr-$ReS_2$/NCBC at 0.5 mV $s^{-1}$. d) The linear relation between $I_p$ and $v^{1/2}$, e) the relation between log($i$) and log($v$), f) the capacitive contribution (pink) and the diffusion contribution (cyan) of dr-$ReS_{2-x}$/NCBC and dr-$ReS_2$/NCBC. g) Normalized proportions of capacitive contributions, h) GITT profiles, and i) diffusion coefficients for dr-$ReS_{2-x}$/NCBC, dr-$ReS_2$/NCBC, $ReS_2$/NCBC.

in Fig. 4e, the *b* values of dr-$ReS_{2-x}$/NCBC for Peak1 and Peak 3 can be determined to be 0.97 and 0.89 when compared with those in dr-$ReS_2$/NCBC (Peak 1: 0.93, Peak 3: 0.83), $ReS_2$/NCBC (Peak 1: 0.86, Peak 3: 0.74), and $ReS_2$ bulk (Peak 1: 0.68, Peak 3: 0.59) (Fig. S14), implying that the electrochemical behaviors in $ReS_2$ based anodes are mainly pseudocapacitive-dominated processes. Moreover, the dr-$ReS_{2-x}$/NCBC exhibits the fastest capacitive kinetics as its highest *b* values, which verifies that the sulfur vacancy could enhance surface capacitive process effectively. Furthermore, the individual capacitive and diffusion contributions can be separated quantitatively at given scan rates, according to the following equations:

$$i = k_1 v + k_2 v^{1/2} \tag{4}$$

$$i/v^{1/2} = k_1 v^{1/2} + k_2 \tag{5}$$

where $k_1 v$ and $k_2 v^{1/2}$ represent the capacitive and diffusion-controlled contributions, respectively. Fig. 4f shows the region ratios for the capacitive contribution in comparison with the diffusion-controlled contribution quantified at 0.5 mV $s^{-1}$. By increasing the scan rate, the capacitive contribution increases whereas the diffusion-controlled contribution is suppressed (Fig. 4g). In particular, the capacitive contribution of dr-$ReS_{2-x}$/NCBC accounts for 71.6% of the total capacity at 0.5 mV $s^{-1}$, which is much higher than that 65.1% of $ReS_2$/NCBC and 61.7% of $ReS_2$/NCBC (Fig. S15), which uncovers the primary cause for its outstanding rate capability. Meanwhile, the galvanostatic intermittent titration technique (GITT) measurements (Fig. 4h) were carried out to reveal the facilitated reaction kinetics in dr-$ReS_{2-x}$/NCBC, with more calculation details in Fig. S17. As shown in Fig. 4i, the diffusion coefficients fluctuate as the potential changes with minimum values appeared in the $D_{Na+}$ versus voltage plots corresponding to redox plateau (Fig. 4h), where the $Na^+$ ions insert/extract the crystalline framework. Notably, the dr-$ReS_{2-x}$/NCBC possesses the highest diffusion coefficient than those in dr-$ReS_2$/NCBC and $ReS_2$/NCBC, indicating its superior diffusion kinetics for $Na^+$ ions.

**First-principles calculations of effect of dual-defect structure.** To gain a better understanding between the dual-defect structure and the enhanced sodium storage behavior, density functional theory (DFT) calculations were conducted with three atomic structures for $ReS_2$, dr-$ReS_2$, and dr-$ReS_{2-x}$ (Figs. S18–20). As their density of states (DOS) shown in Fig. 5a–c, both the interlayer defect and sulfur vacancy in $ReS_2$ could dramatically enhance the electronic conductivity by turning its characteristics from a semiconductor into conductors. In terms of the difference charge density (Fig. 5d and e), the 1D interlayer defect and sulfur vacancy in $ReS_2$ would significantly disturb its charge distribution around the defects, which could be beneficial to providing more active sites for sodium ions for the enhanced electrostatic interactions between $Na^+$ and charge re-distributed defects. After optimizing the structural models of $Na^+$ inserted $ReS_2$, dr-$ReS_2$, and dr-$ReS_{2-x}$ (Fig. 5f), their binding energy values are −0.771, −1.791, and −1.244 eV (Fig. 5g), respectively, demonstrating that the dual-defect structure is energetically conductive to bind $Na^+$. Additionally, Fig. 5h shows the volume changes raised from $Na^+$ insertion in all structures in Fig. 5f. Notably, the dr-$ReS_{2-x}$ shows the lowest volume change of −1.6% after $Na^+$ insertion, when compared to that in dr-$ReS_2$ (3.4%) and $ReS_2$ bulk (5.8%). These data indicate that the introduction of defects can enhance the binding of Na, and reduce the influence of volume change. It should be noticed that the binding of one Na should have attractions to both defective layers, which can reasonably explain the reduce of volume. In

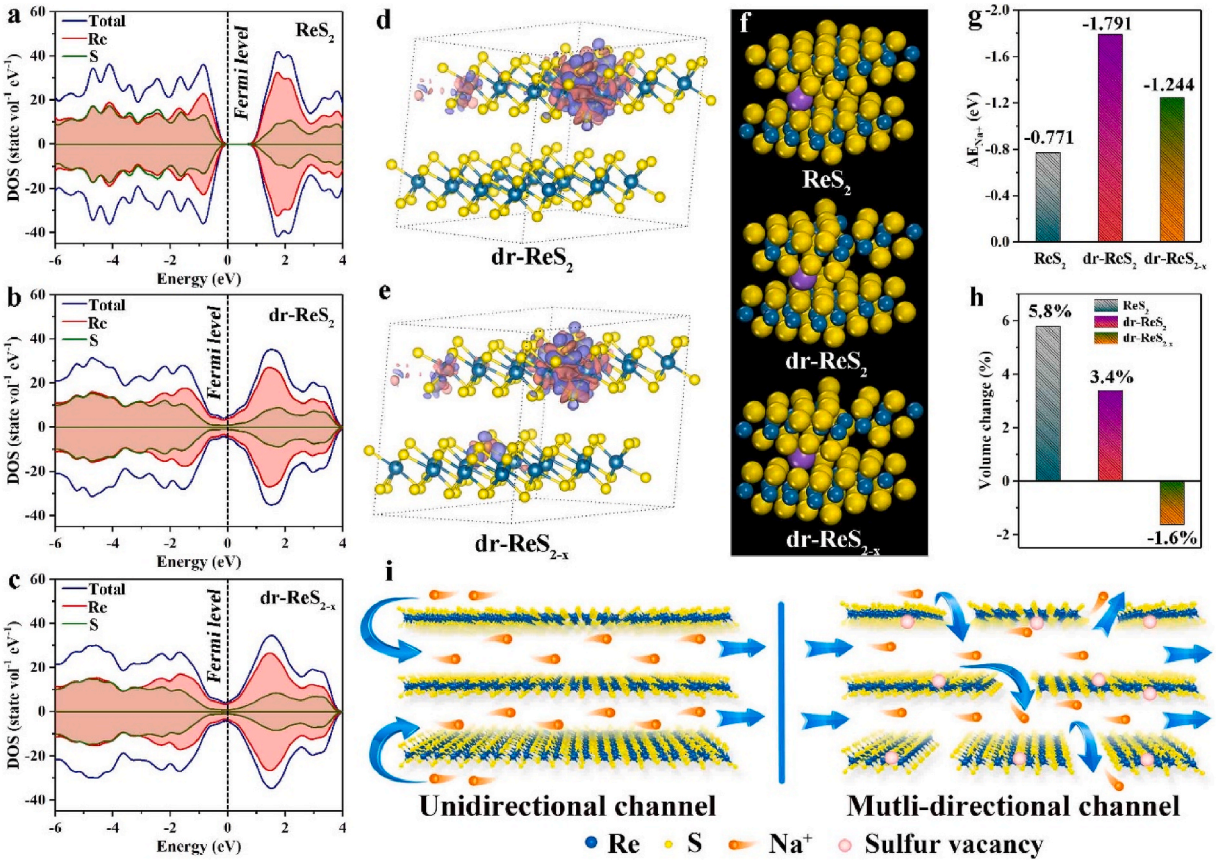


**Fig. 5.** Calculated DOS for a) $ReS_2$, b) dr-$ReS_2$ and c) dr-$ReS_{2-x}$. The difference charge density of d) dr-$ReS_2$ (Pink area, electrons accumulation; Purple area, electrons depletion) and e) dr-$ReS_{2-x}$. f) The atomic models of sodium inserted $ReS_2$, dr-$ReS_2$ and dr-$ReS_{2-x}$. g) Absorption energy values for sodium ions, and h) volume changes after sodium insertion in different models. i) Reaction mechanism for the synergistic effect of interlayer defect and sulfur vacancy.

practice application, a plenty of Na ions in this area would slightly expand the layer distance. Another essential function of interlayer defect in dr-$ReS_{2-x}$ is to shorten the diffusion distance of sodium ions. In detail, the sodium ions can only insert/extract no more than the stack layer edges in $ReS_2$ with unidirectional diffusion pathways, which leads to the inferior rate capacity of $ReS_2$ bulk in Fig. 3c. On the contrary, the interlayer defect breaks the pristine lamellar structure to form interconnected diffusion paths, which creates more potential intercalation sites and shortens the diffusion pathway for sodium ions. It realizes continuous $Na^+$ migration in both vertical and horizontal dimensions, thus efficiently favoring ultrafast $Na^+$ mobility (Fig. 5i).

To confirm the reaction processes and possible crystal evolutions under different voltages during the sodiation/desodiation processes (Fig. 6a), a series of *ex-situ* measurements were carried out, including *ex-situ* HRTEM, XRD, and XPS measurements. For the *ex-situ* HRTEM measurements, the lattice spacing for the (100) plane of dr-$ReS_{2-x}$ crystal (Fig. 6b) increases slightly after discharged to 1.2 V (Fig. 6c), suggesting that sodium ions have been inserted into the interlayers of dr-$ReS_{2-x}$ nanosheets. To go further, two new lattice fringes of 0.21 and 0.23 nm appear after discharged to 0.01 V (Fig. 6d), which can be indexed to the (101) and (220) planes of the metallic Re and $Na_2S$ phases. Finally, the lattice spacing recovers to the pristine state as 0.65 nm corresponding to the (100) plane at fully charged state (Fig. 6e). The crystal structure changes in dr-$ReS_{2-x}$/NCBC were also recorded by *ex-situ* XRD measurements as displayed in Fig. 6f. The (100) plane for $ReS_2$ phase shifts to a smaller angular direction slightly when discharged to 1.2 V. After discharged to 0.01 V, two new characteristic peaks appeared at 27.3° and 39.0°, which can be assigned to the $Na_2S$ phase. Additionally, there is no metallic Re phase observed in the XRD pattern due to the strong diffracted intensities from the copper current collector. As shown in the *ex-situ* XPS spectra (Fig. 6g), the gradual fading of the peak at 42.1 eV (corresponding to $Re^{4+}$ $4f_{7/2}$) and emerging of the new peak at 40.2 eV (corresponding to Re $4f_{7/2}$) when discharged to 0.01 V imply the complete reduction of $ReS_2$ crystal. Therefore, both the *ex-situ* XRD and XPS results confirm well with the as-revealed intercalation mechanism from the *ex-situ* TEM result. Meanwhile, the good impedance reversibility of the dr-$ReS_{2-x}$/NCBC anode from the *ex-situ* EIS measurement (Fig. S21) also reveals the stable phase transition process during cycling process.

**Evaluating performances of full cell device.** To prevent potential safety hazards caused by the high reactivity sodium metal in half cells, we explore the potential of dr-$ReS_{2-x}$/NCBC as an anode in a Na-ion full cell, which was assembled and tested by coupling the dr-$ReS_{2-x}$/NCBC

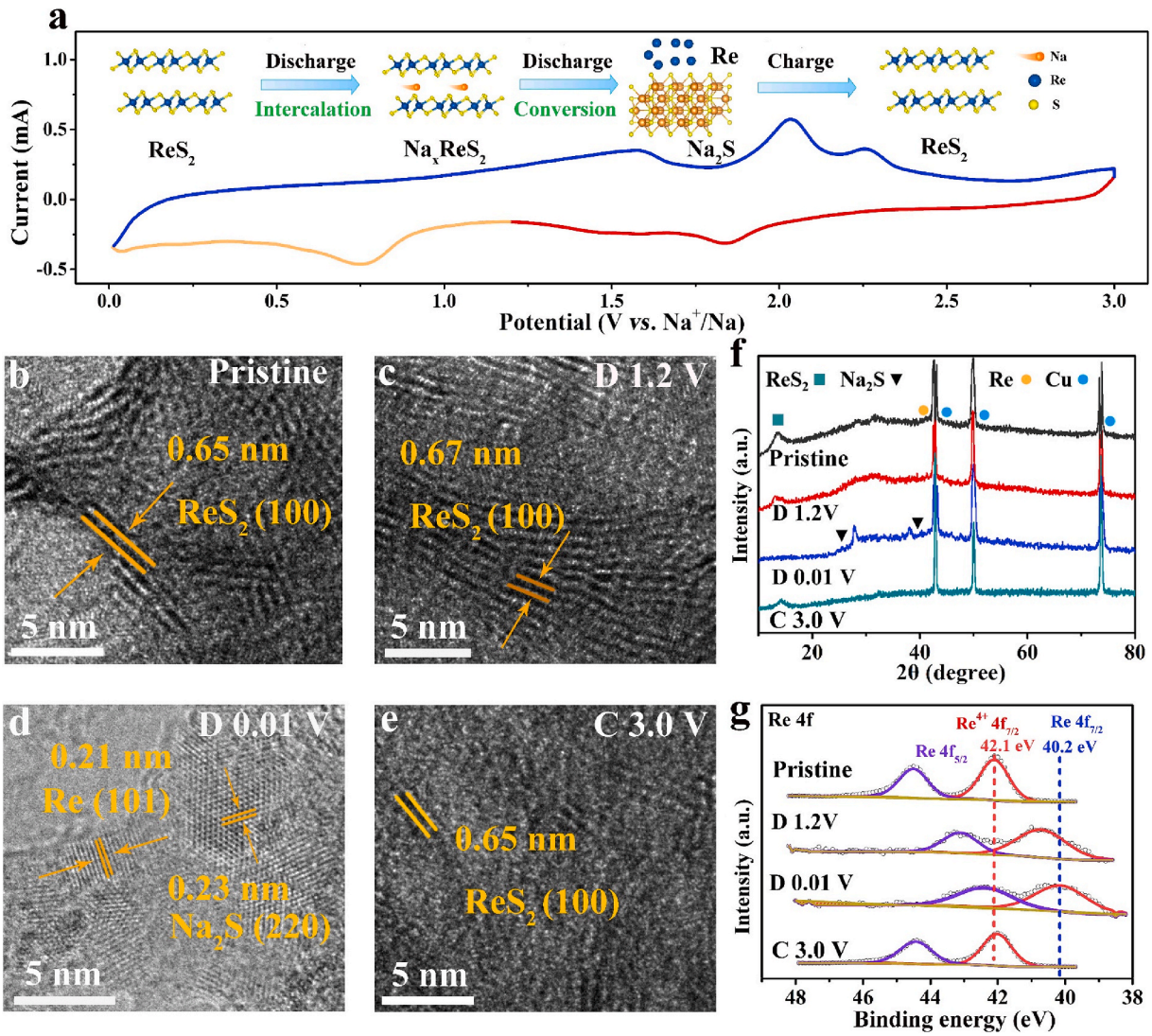


**Fig. 6.** Investigations of the electrochemical process: a) CV curve of dr-$ReS_{2-x}$/NCBC at 0.5 mV $s^{-1}$ (Inset shows the crystal evolution during charging/discharging process). *Ex-situ* HRTEM images of dr-$ReS_{2-x}$/NCBC anode at different states: b) pristine, c) discharged at 1.2 V, d) discharged at 0.01 V, and e) charged at 3 V. f) *Ex-situ* XRD patterns, and g) *ex-situ* XPS spectra of dr-$ReS_{2-x}$/NCBC anodes at different charge/discharge potentials.

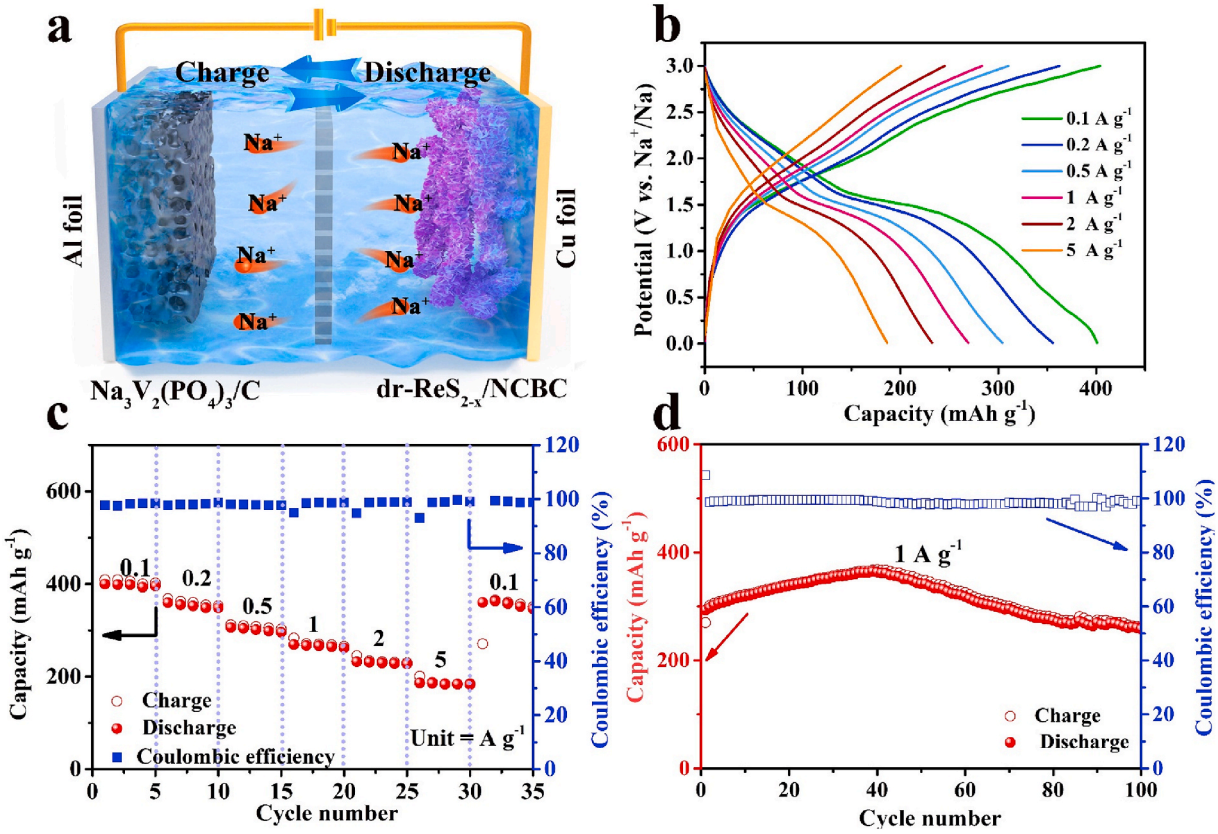


**Fig. 7.** Electrochemical performance of RSN//NVPO full battery: a) Schematic illustration for the sodium-ion full cell assembled with dr-$ReS_{2-x}$/NCBC as anode and $Na_3V_2(PO_4)_3$/C as cathode. b) GCD profiles, c) rate capacity at various current densities, and d) cycling performance at a current density of 1 A $g^{-1}$ of RSN//NVPO full cell battery.

(RSN) anode and $Na_3V_2(PO_4)_3$/C (NVPO) cathode (Fig. 7a). Fig. S22 shows good rate capacity and corresponding GCD curves of $Na_3V_2(PO_4)_3$/C cathode in half cells. As the representative GCD profiles of the RSN//NVPO full cell shown in Fig. 7b, its discharge capacitance values are calculated to be about 401.2, 355.7, 304.1, 269.2, 232.4 and 186.4 mAh $g^{-1}$ as the current density gradually increases from 0.1 to 5 A $g^{-1}$. In addition, Fig. 7c further exhibits the superior rate properties of the RSN//NVPO full cell, its capacitance value returns to 370.2 mAh $g^{-1}$ as the current density gets back to 0.1 A $g^{-1}$. Meanwhile, a discharge capacity of 260.2 mAh $g^{-1}$ can be maintained with a satisfactory capacitance retention of 96.3% at 1 A $g^{-1}$ over 100 cycles, manifesting the excellent stability (Fig. 7d). We further fabricate Li-ion full cells by utilizing RSN anode and $LiCo_2O_4$/C (LCO) cathode. Fig. S23a exhibits the GCD curves of RSN//LCO full cell in the voltage window of 0.8–3.8 V at different current densities (0.1–2 A $g^{-1}$). The RSN//LCO full cell presents superior rate capability in Fig. S23b, where the reversible capacities can be obtained as 587.4, 488.1, 384.5, 287.6 and 175.2 mAh $g^{-1}$ at various current densities from 0.1 to 2 A $g^{-1}$. The capacity can still reach 571.2 mAh $g^{-1}$ when the current density recovers to 0.1 A $g^{-1}$. The RSN//LCO full cell also exhibits excellent cycling stability at 1 A $g^{-1}$ (Fig. S23c), the capacity of which maintains at 191.5 mAh $g^{-1}$ (83.2% of capacity retention) after 400 cycles. The Li/Na-ion full cells present superior rate capability and excellent cycling stability, further proving the potential practical applications of dr-$ReS_{2-x}$/NCBC anode in alkali-ion storage.

## 4. Conclusion

In summary, we successfully prepared interlayer defect, sulfur vacancy-contained $ReS_2$ nanosheets on porous nitrogen-doped carbonized bacterial cellulose (dr-$ReS_{2-x}$/NCBC). The one-dimensional interlayer defects provide multi-dimensional interconnected channels for offering extra pathways of $Na^+$ insertion/extraction and shortening ionic diffusion distance. Additionally, sulfur vacancy could furtherly enhance its electronic conductivity and induce more active sites for sodium-ion storage. As revealed by both experimental and density functional theory calculation results, the enhanced rate capacity (231.2 mAh $g^{-1}$ at 5 A $g^{-1}$) and cycling stability (187.3 mAh $g^{-1}$ at 5 A $g^{-1}$ after 500 cycles) of dr-$ReS_{2-x}$/NCBC are attributed to its favorable electronic structure, negatively shifted binding energy for sodium ions (from −0.771 to −1.791/-1.244 eV), and alleviated structural change (from 5.8% to 3.4%/-1.6%) during sodiation/desodiation processes. The assembled sodium-ion full cell also displays extraordinary sodium storage performance with stable cycle life (capacity retention of 96.3% after 100 cycles) and rate capability (186.4 mAh $g^{-1}$ at 5 A $g^{-1}$). This work is expected to offer an in-depth understanding between dual-defect engineering in TMDs-based anodes and as-enhanced Na-storage performance.

## CRediT authorship contribution statement

**Wei Zong:** Writing - review & editing. **Chao Yang:** Writing - review & editing. **Lulu Mo:** Formal analysis. **Yue Ouyang:** Formal analysis. **Hele Guo:** Writing - review & editing. **Lingfeng Ge:** Writing - review & editing. **Yue-E. Miao:** Resources. **Dewei Rao:** Writing - review & editing. **Jiangwei Zhang:** Supervision. **Feili Lai:** Supervision. **Tianxi Liu:** Supervision.

## Declaration of competing interest

The authors declare that they have no known competing financial interests or personal relationships that could have appeared to influence the work reported in this paper.

## Acknowledgements

We are really grateful for the financial support from the National Natural Science Foundation of China (51433001, 21674019, 21604010), the Science and Technology Commission of Shanghai Municipality (16520722100), the Program of Shanghai Academic Research Leader (17XD1400100), the Shanghai Scientific and Technological Innovation Project (18JC1410600), the "Chenguang Program" supported by Shanghai Education Development Foundation, the Shanghai Scientific and Technological Innovation Project (18JC1410600) and Shanghai Municipal Education Commission (16CG39). We gratefully acknowledge BL14W1 beamline of Shanghai Synchrotron Radiation Facility (SSRF) Shanghai, China for providing the beam time.

## Appendix A. Supplementary data

Supplementary data to this article can be found online at https://doi.org/10.1016/j.nanoen.2020.105189.

## References

[1] B. Dunn, H. Kamath, J.M. Tarascon, Science 334 (2011) 928–935.
[2] M. Armand, J.-M. Tarascon, Nature 451 (2008) 652–657.
[3] H.T. Sun, L. Mei, J.F. Liang, Z.P. Zhao, C. Lee, H.L. Fei, M.N. Ding, J. Lau, M.F. Li, C. Wang, X. Xu, G.L. Hao, B. Papandrea, I. Shakir, B. Dunn, Y. Huang, X.F. Duan, Science 356 (2017) 599–604.
[4] Y.X. Huang, L.Z. Zhao, L. Li, M. Xie, F. Wu, R.J. Chen, Adv. Mater. 31 (2019) 1808393.
[5] J.W. Choi, D. Aurbach, Nat. Rev. Mater. 1 (2016) 16013.
[6] C. Yang, J.R. Feng, F. Lv, J.H. Zhou, C.F. Lin, K. Wang, Y.L. Zhang, Y. Yang, W. Wang, J.B. Li, S.J. Guo, Adv. Mater. 30 (2018) 1800036.
[7] Z.Q. Zhu, Y.X. Tang, W.R. Leow, H.R. Xia, Z.S. Lv, J.Q. Wei, X. Ge, S.K. Cao, Y. Y. Zhang, W.H. Zhang, S.B. Xi, Y.H. Du, X.D. Chen, Angew. Chem. Int. Ed. 58 (2019) 3521–3526.
[8] H.T. Tan, Y.Z. Feng, X.H. Rui, Y. Yan, S.M. Huang, Small Methods 4 (2020) 1900563.
[9] Z.Q. Zhu, Y.X. Tang, Z.S. Lv, J.Q. Wei, Y.Y. Zhang, R.S. Wang, W. Zhang, H.R. Xia, M.Z. Ge, X.D. Chen, Angew. Chem. Int. Ed. 57 (2018) 3656–3660.
[10] L. Li, Y. Zheng, S. Zhang, J. Yang, Z.P. Shao, Z.P. Guo, Energy Environ. Sci. 11 (2018) 2310–2340.
[11] W. Luo, F. Shen, C. Bommier, H.L. Zhu, X.L. Ji, L.B. Hu, Acc. Chem. Res. 49 (2016) 231–240.
[12] L. Li, W.C. Zhang, X. Wang, S.L. Zhang, Y.J. Liu, M.H. Li, G.J. Zhu, Y. Zheng, Q. Zhang, T. Zhou, W.K. Pang, W. Luo, Z.P. Guo, J.P. Yang, ACS Nano 13 (2019) 7939–7948.
[13] L. Li, W.C. Zhang, X. Wang, S.L. Zhang, Y.J. Liu, M.H. Li, G.J. Zhu, Y. Zheng, Q. Zhang, T. Zhou, W.K. Pang, W. Luo, Z.P. Guo, J.P. Yang, Adv. Mater. 30 (2018) 1801013.
[14] F.E. Niu, J. Yang, N.N. Wang, D.P. Zhang, W.L. Fan, J. Yang, Y.T. Qian, Adv. Funct. Mater. 27 (2017) 1700522.
[15] N. Feng, R. Meng, L. Zu, Y. Feng, C. Peng, J. Huang, G. Liu, B. Chen, J. Yang, Nat. Commun. 10 (2019) 1372.
[16] L.M. Zhou, Q. Liu, Z.H. Zhang, K. Zhang, F.Y. Xiong, S.S. Tan, Q.Y. An, Y.M. Kang, Z. Zhou, L.Q. Mai, Adv. Mater. 30 (2018) 1801984.
[17] G.Y. Zhou, Y.-E. Miao, Z.X. Wei, L.L. Mo, F.L. Lai, Y. Wu, J.M. Ma, T.X. Liu, Adv. Funct. Mater. 28 (2018) 1804629.
[18] C.S. Yan, C.D. Lv, Y. Zhu, G. Chen, J.X. Sun, G.H. Yu, Adv. Mater. 29 (2017) 1703909.
[19] J.H. Liu, J.S. Chen, X.F. Wei, X.W. Lou, X.W. Liu, Adv. Mater. 23 (2011) 998–1002.
[20] G.Z. Fang, Q.C. Wang, J. Zhou, Y.P. Lei, Z.X. Chen, Z.P. Wang, A.Q. Pan, S.Q. Liang, ACS Nano 13 (2019) 5635–5645.
[21] P. Ge, S.J. Li, H.L. Shuai, W. Xu, Y. Tian, L. Yang, G.Q. Zou, H.S. Hou, X.B. Ji, Adv. Mater. 31 (2019) 1806092.
[22] J. Bao, X.D. Zhang, B. Fan, J.J. Zhang, M. Zhou, W.L. Yang, X. Hu, H. Wang, B. C. Pan, Y. Xie, Angew. Chem. Int. Ed. 54 (2015) 7399–7404.
[23] Y. Jia, K. Jiang, H. Wang, X.D. Yao, Chem 5 (2019) 1371–1397.
[24] L.Z. Zhuang, L. Ge, Y.S. Yang, M.R. Li, Y. Jia, X.D. Yao, Z.H. Zhu, Adv. Mater. 29 (2017) 1606793.
[25] H. Wang, D. Yong, S.C. Chen, S.L. Jiang, X.D. Zhang, W. Shao, Q. Zhang, W.S. Yan, B.C. Pan, Y. Xie, J. Am. Chem. Soc. 140 (2018) 1760–1766.
[26] J. Mei, Y. Zhang, T. Liao, Z.Q. Sun, S.X. Dou, Natl. Sci. Rev. 5 (2018) 389–416.
[27] Y. Zhang, Z.Y. Ding, C.W. Foster, C.E. Banks, X.Q. Qiu, X.B. Ji, Adv. Funct. Mater. 27 (2017) 1700856.
[28] Y.H. Zou, W. Zhang, N. Chen, S. Chen, W.J. Xu, R.S. Cai, C.L. Brown, D.J. Yang, X. D. Yao, ACS Nano 13 (2019) 2062–2071.
[29] J. Liang, Z.X. Wei, C. Wang, J.M. Ma, Electrochim. Acta 285 (2018) 301–308.
[30] F.L. Lai, N. Chen, X.B. Ye, G.J. He, W. Zong, K.B. Holt, B.C. Pan, I.P. Parkin, T. X. Liu, R.J. Chen, Adv. Funct. Mater. 30 (2020) 1907376.
[31] Q. Zhang, S.J. Tan, R.G. Mendes, Z.T. Sun, Y.T. Chen, X. Kong, Y.H. Xue, M. H. Rummeli, X. Wu, S.L. Chen, L. Fu, Adv. Mater. 28 (2016) 2616–2623.
[32] S.J. Deng, Y. Zhang, D. Xie, L. Yang, G.Z. Wang, X.S. Zheng, J.F. Zhu, X.L. Wang, Y. Yu, G.X. Pan, X.H. Xia, J.P. Tu, Nano Energy 58 (2019) 355–364.
[33] H.Y. Li, Z. Cheng, Q. Zhang, A. Natan, Y. Yang, D.X. Cao, H.L. Zhu, Nano Lett. 18 (2018) 7407–7413.
[34] H.F. Shi, Z.H. Sun, W. Lv, S.G. Wang, Y. Shi, Y.B. Zhang, S.J. Xiao, H.C. Yang, Q.-H. Yang, F. Li, J. Mater. Chem. A 7 (2019) 11298–11304.
[35] G. Kresse, J. Furthmüller, Phys. Rev. B 54 (1996) 11169.
[36] G. Kresse, J. Hafner, Phys. Rev. B 48 (1993) 13115.
[37] G. Kresse, J. Furthmüller, Comput. Mater. Sci. 6 (1996) 15–50.
[38] J.P. Perdew, K. Burke, M. Ernzerhof, Phys. Rev. Lett. 77 (1996) 3865.
[39] P.E. Blochl, Phys. Rev. B 50 (1994) 17953.
[40] Q.Y. Xia, H. Yang, M. Wang, M. Yang, Q.B. Guo, L.M. Wan, H. Xia, Y. Yu, Adv. Energy Mater. 7 (2017) 1701336.
[41] W. Zong, F.L. Lai, G.J. He, J.R. Feng, W. Wang, R.Q. Lian, Y.E. Miao, G.C. Wang, Small 14 (2018) 1801562.
[42] X. Sun, X. Luo, X. Zhang, J. Xie, S. Jin, H. Wang, X. Zheng, X. Wu, Y. Xie, J. Am. Chem. Soc. 141 (2019) 3797–3801.
[43] X. Wang, Y.W. Zhang, H.N. Si, Q.H. Zhang, J. Wu, L. Gao, X.F. Wei, Y. Sun, Q. L. Liao, Z. Zhang, K. Ammarah, L. Gu, Z. Kang, Y. Zhang, J. Am. Chem. Soc. 142 (2020) 4298–4308.
[44] F.L. Lai, W. Zong, G.J. He, Y. Xu, H.W. Huang, B. Weng, D.W. Rao, J.A. Martens, J. Hofkens, I.P. Parkin, T.X. Liu, Angew. Chem. Int. Ed. (2020), https://doi.org/10.1002/anie.202003129.
[45] H.N. He, D. Huang, Q.M. Gan, J.N. Hao, S.L. Liu, Z.B. Wu, W.K. Pang, B. Johannessen, Y.G. Tang, J.L. Luo, H.Y. Wang, Z.P. Guo, ACS Nano 13 (2019) 11843–11852.
[46] F.C. Lei, Y.F. Sun, K.T. Liu, S. Gao, L. Liang, B.C. Pan, Y. Xie, J. Am. Chem. Soc. 136 (2014) 6826–6829.
[47] Z.C. Lai, A. Chaturvedi, Y. Wang, T.H. Tran, X.Z. Liu, C.L. Tan, Z.M. Luo, B. Chen, Y. Huang, G.H. Nam, Z.C. Zhang, Y. Chen, Z.N. Hu, B. Li, S.B. Xi, Q.H. Zhang, Y. Zong, L. Gu, C. Kloc, Y.H. Du, H. Zhang, J. Am. Chem. Soc. 140 (2018) 8563–8568.
[48] T.T. Zheng, C.Y. Shang, Z.H. He, X.Y. Wang, C. Cao, H.L. Li, R. Si, B.C. Pan, S. M. Zhou, J. Zeng, Angew. Chem. Int. Ed. 58 (2019) 14764–14769.
[49] B. Chen, H. Li, H.X. Liu, X.Q. Wang, F.X. Xie, Y.D. Deng, W.B. Hu, K. Davey, N. Q. Zhao, S.Z. Qiao, Adv. Energy Mater. 9 (2019) 1901146.
[50] S. Liu, Y. Liu, W.W. Lei, X. Zhou, K. Xu, Q.Q. Qiao, W.H. Zhang, J. Mater. Chem. A 6 (2018) 20267–20276.
[51] X.Q. Wang, B. Chen, J. Mao, J.W. Sha, L.Y. Ma, N.Q. Zhao, F. He, Electrochim. Acta 338 (2020) 135695.
[52] X.E. Zhang, C. Shen, H.Y. Wu, Y. Han, X.Y. Wu, W.R. Ding, L.B. Ni, G.W. Diao, M. Chen, Energy Storage Mater. 26 (2020) 457–464.
[53] Y. Von Lim, S.Z. Huang, Q.Y. Wu, Y.M. Zhang, D.Z. Kong, Y. Wang, T.T. Xu, Y. M. Shi, Q. Ge, L.K. Ang, H.Y. Yang, Nano Energy 61 (2019) 626–636.
[54] X.Q. Xiong, W. Luo, X.L. Hu, C.J. Chen, L. Qie, D.F. Hou, Y.H. Huang, Sci. Rep. 5 (2015) 9254.
[55] Z.-H. Zhao, X.-D. Hu, H.Q. Wang, M.-Y. Ye, Z.-Y. Sang, H.-M. Ji, X.-L. Li, Y.J. Dai, Nano Energy 48 (2018) 526–535.
[56] Y. Li, R.P. Zhang, W. Zhou, X. Wu, H.B. Zhang, J. Zhang, ACS Nano 13 (2019) 5533–5540.
[57] M. Yousaf, Y.S. Wang, Y.J. Chen, Z.P. Wang, A. Firdous, Z. Ali, N. Mahmood, R. Q. Zou, S.J. Guo, R.P. Han, Adv. Energy Mater. 9 (2019) 1900567.
[58] X. Li, Y.G. Sun, X. Xu, Y.-X. Wang, S.-L. Chou, A.M. Cao, L.B. Chen, S.-X. Dou, J. Mater. Chem. A 7 (2019) 25932–25943.
[59] H.M. Qi, L.N. Wang, T.T. Zuo, S.L. Deng, Q. Li, Z.-H. Liu, P. Hu, X.X. He, ChemElectroChem 7 (2020) 78–85.

**Wei Zong** received his B.S. degree from Ludong University (2017). Now he is a Ph.D. candidate in College of Materials Science and Engineering, Donghua University. His current research interests include design and synthesis of advanced nanostructured materials for Li/Na/K-ion batteries and supercapacitor.

**Chao Yang** received his M.Sc. degree from Hainan University in 2018. During 2016 and 2018, he studied at Peking University as a joint M.Sc. student. He is now a Ph.D. candidate in Technische Universität Berlin. His research interests include the design, synthesis and characterization of advanced energy materials for Li/Na/K-ion batteries, solid-state electrolyte and catalysis.

**Lulu Mo** received her Master's degree in Chemistry from Henan University of Technology in 2017. Currently, she is a Ph. D. candidate in College of Materials Science and Engineering, Donghua University. Her research focuses on the design and preparation of nanostructured electrode materials for sodium ion batteries.

**Yue Ouyang** received her B.S. degree from Donghua University (2017). Now she is a Ph.D. candidate in College of Materials Science and Engineering, Donghua University. Her research focuses on design and preparation of high-performance carbon nanofiber composites in Li–S and Li-metal batteries.

**Hele Guo** received his B.S. degree from Donghua University, Shanghai, P. R. China (2017). He received his M.D. degree under the supervision of Prof. Chao Zhang and Prof. Tianxi Liu in Donghua University, Shanghai, P. R. China. His research interests include controllable preparation and electrocatalytic properties of carbon hybrid materials.

**Lingfeng Ge** earned her Bachelor of Science from Xiamen University (Xiamen, China). Later She attended two one-year master's programmes and obtained a master's degree from each-one is Master of Science from the University of Manchester (Manchester, UK) and the other is Master Sciences, Technologies, Sante from Universite Paris Descartes and Universite Paris Diderot (Paris, France). Now she is studying for a PhD in Physical Chemistry at the University of Bristol (Bristol, UK).

**Yue-E Miao** received her B.S. degree from Southeast University in 2010 and Ph.D. degree from Fudan University in 2015. She is now an associate professor of School of Materials Science and Engineering at Donghua University. Her research interests mainly focus on high-performance organic fiber electrodes/separators, carbon nanofiber composites, as well as their applications in electrochemical energy storage devices (such as Li/Na-ion batteries, and Li–S batteries).

**Dewei Rao** received the B.S. degree in applied physics and Ph. D. degree in materials science and engineering from the Nanjing University of Science & Technology, in 2007 and 2013, respectively. He is now a staff of the School of Materials Science and Engineering, Jiangsu University. His research interests include designing electrodes of advanced batteries and electrocatalysts, and understanding the mechanisms of experimental results through density functional theory calculations and molecular simulations.

**Jiangwei Zhang** is currently a associate research fellow of Dalian National Laboratory for Clean Energy & State Key Laboratory of Catalysis, Dalian Institute of Chemical Physics. He received his B.S. from Beijing University of Chemical Technology in 2011 and his Ph.D. from Department of Chemistry, Tsinghua University in 2016. Currently, His researches focus atomically precise material structure determination and their corresponding catalytic applications in cutting edge of energy-related filed.

**Feili Lai** received his BE degree from Donghua University (2014), master degree from Fudan University (2017), and Ph. D. degree from Max Planck Institute of Colloids and Interfaces/Universität Potsdam (2019). He is now a research fellow of the Department of Chemistry, KU Leuven. His current interests include the machine learning in materials science, the design and synthesis of low-dimensional solids for energy storage and conversion applications.

**Prof. Tianxi Liu** obtained his BS degree from Henan University (1992) and Ph.D. degree from Changchun Institute of Applied Chemistry, Chinese Academy of Sciences (1998). He is currently a full professor in Jiangnan University. His main research interests include polymer nanocomposites, organic/inorganic hybrid materials, nanofibers and their composites, advanced energy materials for energy conversion and storage.